Nano Research
2021, 14(5): 1533–1540

ISSN 1998-0124 CN 11-5974/O4
https://doi.org/10.1007/s12274-020-3212-z

Research Article

Bimetallic metal-organic framework derived doped carbon nanostructures as high-performance electrocatalyst towards oxygen reactions

Lu Chen[1,2], Zhi Chen[2] (✉), Xudong Liu[1], and Xiaolei Wang[1,3] (✉)

[1] *Department of Chemical and Materials Engineering, Concordia University, Montreal, Quebec H3G 1M8, Canada*
[2] *Department of Building, Civil and Environmental Engineering, Concordia University, Montreal, Quebec H3G 1M8, Canada*
[3] *Department of Chemical and Materials Engineering, University of Alberta, Edmonton, Alberta T6G 1H9, Canada*

© Tsinghua University Press and Springer-Verlag GmbH Germany, part of Springer Nature 2020
Received: 16 September 2020 / **Revised:** 16 October 2020 / **Accepted:** 26 October 2020

ABSTRACT

Rational design and development of cost-effective, highly active and durable bifunctional electrocatalysts towards oxygen redox reactions is of critical importance but great challenge for the broad implementation of next-generation metal-air batteries for electric transportation. Herein, a high-performance electrocatalyst of cobalt and zinc sulfides nanocrystals embedded within nitrogen and sulfur co-doped porous carbon is successfully designed and derived from bimetallic metal-organic frameworks of cobalt and zinc containing zeolitic imidazolate frameworks. The unique nanostructure contains abundant electrocatalytic active sites of sulfides nanocrystals and nitrogen and sulfur dopants which can be fast accessed through highly porous structure originate from both zinc vaporization and sulfurization processes. Such bifunctional electrocatalyst delivers a superior half-wave potential of 0.86 V towards oxygen reduction reaction and overpotential of 350 mV towards oxygen evolution reaction, as well as excellent durability owing to the highly stable carbon framework with a great graphitized portion. The performance boosting is mainly attributed to the unique nanostructure where bimetallic cobalt and zinc provide synergistic effect during both synthesis and catalysis processes. The design and realization pave a new way of development and understanding of bifunctional electrocatalyst towards clean electrochemical energy technologies.

KEYWORDS

bimetallic metal-organic frameworks, carbon nanostructures, electrocatalysts, oxygen redox reactions, nitrogen and sulfur doping

1 Introduction

An exponential growth of energy consumption results in the fast depletion of fossil fuels and severe deterioration of environment, which in turn stimulates the discovery and development of renewable and sustainable energy technologies [1]. Over the past decades, electrochemical energy storage and conversion systems have been emerging as the most promising candidate in renewable energy sector, including fuel cells, rechargeable lithium-ion batteries (LIBs) and supercapacitors, etc. [2]. Particularly, metal-air batteries are widely believed to be the next-generation power source due to their high theoretical energy density often a magnitude greater than that of LIBs, abundant feed (air), as well as reliable and safe operations [3]. However, their implementation towards electric vehicles and grid storage applications is still hindered by the inherently sluggish kinetics and consequent high overpotential and complex multiple reactions [4]. More specifically, electrochemical oxygen redox reactions (i.e., oxygen reduction reaction (ORR) and oxygen evolution reactions (OER)) need significantly improved [5–7]. So far, noble-metal based materials, such as ruthenium oxide (RuO_2) [8], iridium oxide (IrO_2) [9], and platinum (Pt) [10] are found to be the most efficient OER and ORR electrocatalysts. Unfortunately, their limited reserves and uneven distribution resulted high price, easy aggregation and deactivation resulted poor stability place a major hurdle to the broad commercialization [11–13]. Hence, replacement of these noble-metal based electrocatalysts in metal-air batteries with low-cost and high-performance electrocatalyst is the key to the next-generation electrochemical energy technologies.

To date, many transition metal compounds including oxide (e.g., Co_3O_4), sulfide (e.g., MoS_2), phosphide (e.g., NiP), and carbon-based materials (e.g., N-doped graphene) have been extensively investigated for OER and ORR, respectively; while efficient combination of ORR and OER electrocatalysts facilitates the fabrication and integration of metal-air battery devices [14–16]. For example, Co_3O_4 nanocrystals embedded porous carbon spheres with pomegranate-like architecture exhibit both ORR and OER electrocatalytic behavior, and such bifunctional electrocatalyst-based zinc-air battery prototype shows excellent device performance [17]. Generally, a high-performance oxygen electrocatalyst should possess several key features: i) abundant highly active sites for oxygen redox; ii) fast access to active sites for reactants and conductive networks for efficient electron transfer; iii) stable material structure and well-defined interfaces for durability.

Address correspondence to Xiaolei Wang, xiaolei.wang@ualberta.ca; Zhi Chen, zhi.chen@concordia.ca

Recently, metal organic frameworks (MOFs) have been reported promising for electrocatalysts as either precursors or sacrificial templates due to their highly porous feature, various morphologies, tunable compositions by engineering different metal ions and organic ligands [18, 19]. MOFs derived nanostructures are expected to possess all desired features that favor electrocatalytic oxygen reactions [20–22]. As a representative in MOFs family, zeolitic imidazolate frameworks (ZIFs) with its special structure where metal atoms and other elements are integrated into carbon skeleton have been already studied to fabricate nano-scale porous carbon materials for oxygen electrocatalysts [23–26]. For example, Zhang et al. synthesized NiFe-LDH/Co,N-CNF composites which displayed an OER overpotential of 0.312 V at 10 mA·cm^{-2} and an ORR half-wave potential of 0.790 V [27]; while Co@NC-*x*/*y* was derived from pyrolysis of Co/Zn-ZIF and showed the superb ORR activity with onset potential of 1.15 V and half wave potential of 0.93 V [28]. Ma et al. reported ZIF-67/PAN fiber that exhibited excellent bifunctional electrocatalytic activity [29]. Although performance improvement has been achieved, MOFs, especially ZIFs-derived electrocatalysts are still hard to outperform those noble metals for ORR and OER [30, 31]. On the other hand, systematic study of catalytic mechanisms originated from element doping and change of local electronic structure of transition metals is insufficient [32]. Heteroatoms doping in carbon based materials including S [33], P [34], and B [35] enables extra active sites, improved conductivity and tunable structure [36, 37]. For instance, Fe/N/S-CNTs derived from ZIF-8 exhibited superior ORR performance, which was ascribed to sulfate ions creating C–S–C bonds by reaction with carbon at a high temperature [36]. Cu_3P@NPPC with uniformed N and P doping synthesized from Cu-based MOFs showed excellent ORR performance due to synergistic effects between Cu_3P and doped carbon [37]. Nevertheless, further creation and understanding of such synergistic effect at molecular level are strongly demanded.

Herein, we demonstrate a unique nanostructure of N and S codoped porous carbon (N,S-Co/Zn-ZIF) derived from bimetallic ZIFs. As shown in Scheme 1, Co/Zn containing ZIF-67 (Co/Zn-ZIF-67) precursor is prepared by a simple precipitation method where cobalt and zinc ions can coordinate with ligand links; while a facile one-step calcination and sulfurization directly converts Co/Zn-ZIF-67 precursor into N,S-Co/Zn-ZIF. Such electrocatalyst possesses a well-defined porous dodecahedron morphology and exhibits outstanding OER and ORR electrocatalytic performance. The bimetallic ZIFs provide more interactions between transition metals with doped N and S atoms and consequently create more synergistic catalytic effects. Moreover, existence of both Co and Zn protects rhombic dodecahedron morphology from decomposing after calcination. In addition, coordination effects between carbon matrix and Co/Zn compounds nanoclusters improve the contact between the nanostructure and the electrolyte, leading to an excellent OER performance with overpotential of 350 mV and ORR activity with half-wave potential of 0.86 V at 1,600 rpm. The design and realization of such nanostructured material derived from bimetallic ZIFs pave a new way of development and understanding of bifunctional electrocatalysts towards clean electrochemical energy technologies.

2 Results and discussion

2.1 Morphology characterization

Highly porous N,S-Co/Zn-ZIF was successfully synthesized from bimetallic Co/Zn containing ZIF-67 (Co/Zn-ZIF-67) precursor which also possesses a rhombic dodecahedron morphology with smooth surface and a particle size of around 500 nm (Fig. S1 in the Electronic Supplementary Material (ESM)). After one-step calcination and sulfurization treatment, the nanostructured electrocatalyst of N,S-Co/Zn-ZIF was achieved. The morphology and structure of N,S-Co/Zn-ZIF are characterized by scanning electron microscopy (SEM) and transmission electron microscopy (TEM). As shown in Fig. 1(a) nanostructured N,S-Co/Zn-ZIF maintains the same rhombic dodecahedron morphology as Co/Zn-ZIF-67 but exhibits rough surface after the calcination and sulfurization (Fig. 1(b)). The existence of bimetallic Co and Zn plays an important role in maintaining the morphology and developing porous structure of N,S-Co/Zn-ZIF. Although N,S-Co-ZIF still shows a rhombic dodecahedron morphology (Figs. S2(a) and S2(b) in the ESM), the existence of single metal results in the morphology decomposition. Also, the existence of only Zn leads to nanospheres with an average size of around 100 nm (Figs. S2(c) and S2(d) in the ESM). Moreover, due to its low boiling point, Zn containing compounds evaporate during calcination at high temperature, forming porous structure that can be reflected by the rough surface [38]. Thus, more active sites are created and exposed that facilitate electrocatalytic process. In addition, without sulfurization, nanofibers are inevitably formed, while the rhombic dodecahedron morphology is also hard to be defined (Figs. S2(e) and S2(f) in the ESM).

The highly porous nanostructure of N,S-Co/Zn-ZIF is clearly revealed by TEM images in Fig. 1(c). The nanostructure is composed of nanoparticles implying the conversion of bimetallic Co and Zn precursors into their compounds embedded within the derived porous carbon. The high-resolution TEM (HRTEM) images in Fig. 1(d) confirm the existence of metal sulfides with an average size of 25 nm, which is consistent with the selected area electron diffraction (SAED) observation in Fig. 1(e). Moreover, the carbon nanostructure is highly graphitized with an inter-lattice spacing of 0.34 nm, forming a highly conductive network for fast electrons transfer. The lattice fringes with an inter-planar spacing of 0.31 and 0.16 nm can be perfectly indexed to (111) and (311) crystal planes of the $Zn_{0.76}Co_{0.24}S$, while the lattice spacings of 0.19 and 0.24 nm are ascribed to the (110) and (101) planes of ZnS and $Co_{1-x}S_x$, respectively. The presence of bimetallic sulfides nanoparticles embedded within derived carbon nanostructure is further confirmed by high-angle annular dark-field (HAADF)-scanning transmission electron microscopy (STEM) image in

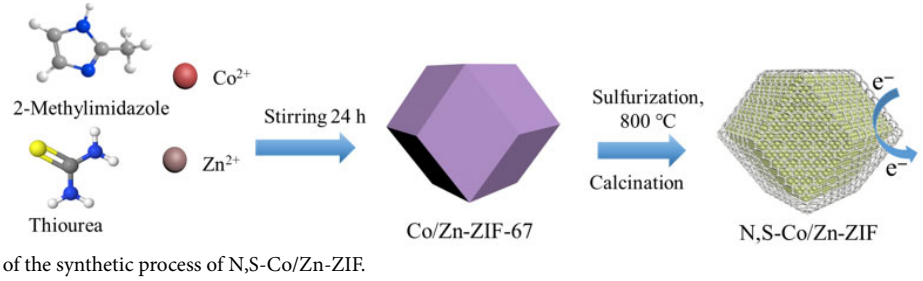

Scheme 1 Schematic of the synthetic process of N,S-Co/Zn-ZIF.

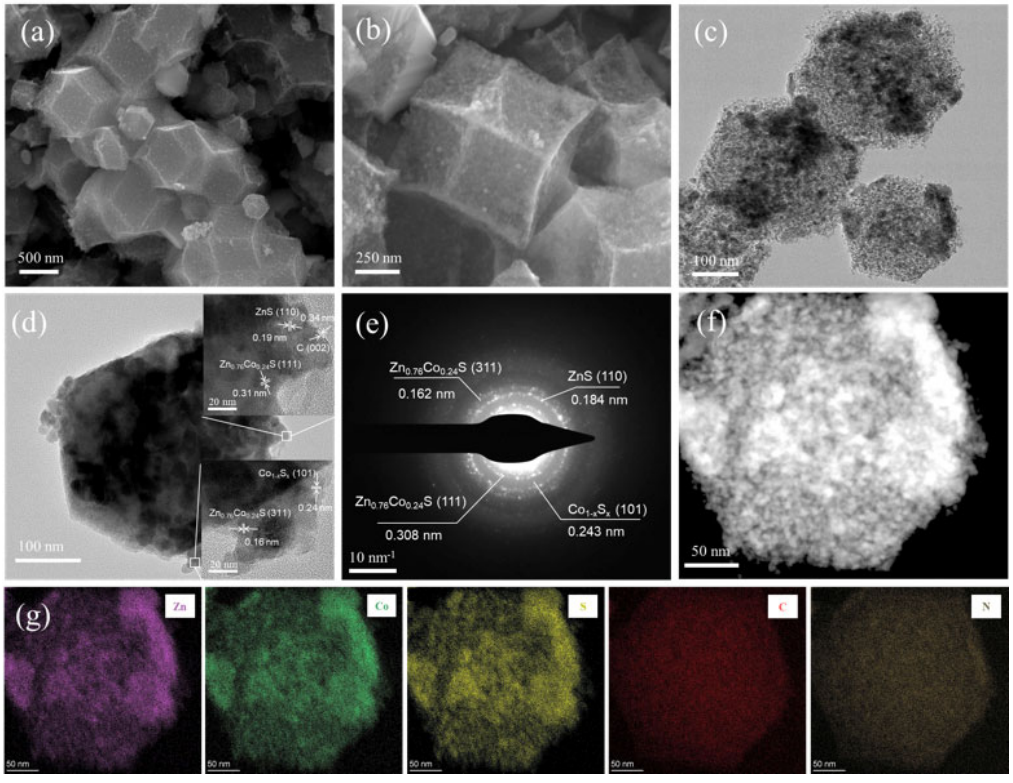

Figure 1 (a) Low and (b) high magnification SEM images of as-synthesized N,S-Co/Zn-ZIF. (c) TEM image of N,S-Co/Zn-ZIF nanoparticles. (d) TEM image of a single N,S-Co/Zn-ZIF nanoparticle (inset: HRTEM images of two selected areas). (e) The corresponding SAED pattern recorded from a single nanoparticle. (f) HAADF-STEM image of a single N,S-Co/Zn-ZIF; and (g) the corresponding EDS element mapping spectra of element Zn, Co, S, C and N.

Fig. 1(f). All of the elements Co, Zn, C, N, and S are uniformly distributed in the dodecahedra cluster in Fig. 1(g).

2.2 Structural analysis

The crystal structures of transition metal compounds were analyzed by X-ray diffraction (XRD) technique. The Rietveld refinement of N,S-Co/Zn-ZIF can be perfectly fitted to the diffraction pattern with excellent agreement factors (R_{wp} = 3.90%, R_p = 7.91%) (Fig. 2(a)). It demonstrates a dominant cubic system of $Zn_{0.76}Co_{0.24}S$ (JCPDS No. 47-1656) in N,S-Co/Zn-ZIF with a high phase content of 85.3 wt.%, while small amount of ZnS (11.1 wt.%, JCPDS No. 36-1450) and $Co_{1-x}S_x$ (3.6 wt.%, JCPDS No. 42-0826) coexist. By comparison, as-synthesized N,S-Co-ZIF, N,S-Zn-ZIF and Co/Zn-ZIF show different phases (Fig. S3 in the ESM), where the crystallographic parameters are illustrated in Table S1 in the ESM. Such XRD results are in good agreement with the HRTEM observations where ultrafine $Zn_{0.76}Co_{0.24}S$ nanocrystals are dominantly embedded in ZIF-derived porous carbon. The porous structure of N,S-Co/Zn-ZIF nanostructure was investigated by nitrogen adsorption/desorption isotherms. Type IV isotherms can be obtained with an identifiable hysteresis loop (Fig. 2(b)), which indicates a dominant mesoporous structure with a high Brunauer–Emmett–Teller (BET) surface area of 197.8 $m^2 \cdot g^{-1}$. The pore size distribution is calculated by the Barrett–Joyner–Halenda (BJH) method, which describes the majority of mesopores of 24.5 nm. It can be concluded that the synthesis transforms bimetallic Co/Zn-ZIF-67 into a hierarchically porous structure with abundant pore channels, which facilitates the ion and molecule transportation [39].

The elemental composition and electronic structure of N,S-Co/Zn-ZIF nanostructure were investigated by X-ray photoelectron spectroscopy (XPS) analysis. The complete survey spectrum demonstrates the existence of Zn, Co, S, C, and N (Fig. S4 in the ESM). The elemental ratios measured by XPS spectroscopy agree well with the results of energy-dispersive X-ray (EDX) spectrum (Table S2 in the ESM). From the Zn 2p region exhibited in Fig. 2(c), the two main peaks observed at 1,044.84 and 1,021.74 eV belong to Zn $2p_{1/2}$ and Zn $2p_{3/2}$, respectively, which corresponds to the Zn^{2+} [32]. As for the Co 2p spectrum in Fig. 2(d), the main peaks at 780.48, 796.48 eV and 778.38, 793.38 eV demonstrate the co-existence of Co^{2+} and Co^{3+}, which is consistence with XRD and HRTEM analysis. In addition to the binding energy of C=O at 288.15 eV and C–C at 284.71 eV [40, 41], C–N at 285.78 eV and C–S peak located at 286.25 eV in C 1s spectrum (Fig. 2(e)) confirm the S and N doping in the C matrix. This indicates that N is distributed almost entirely on the carbon surface, which verifies the incorporation of N in the carbon matrix [42]. As depicts in Tables S2 and S3 in the ESM, the amount of N element is higher in N,S-Co/Zn-ZIF (≈ 11.25 at.%) than Co/Zn-ZIF (≈ 9.55 at.%), owing to the thiourea in the precursor and thermal decomposition during pyrolysis [43]. N 1s spectrum proves the existence of the pyridinic N (398.78 eV), pyrrolic N (400.01 eV), graphitic N (400.88 eV), and oxide N (402.68 eV), as shown in Fig. 2(f) [44, 45]. It is reported that graphite and pyridine N are considered playing an essential role in prompting the catalytic ability for ORR and OER [12]. In S 2p spectrum (Fig. 2(g)), the two peaks located at 162.28 and 163.88 eV are ascribed to the S $2p_{1/2}$ and S $2p_{3/2}$ of Zn-S bond, while the other two peaks at 162.88 and 161.58 eV can be attributed to the S $2p_{1/2}$ and S $2p_{3/2}$ of the Co-S bond [46, 47], which indicating the successful sulfurization on the Co/Zn-ZIF-67 precursor. The S element are both from thiourea and S powder from the vulcanization process. However, thiourea can be easily decomposed into gas during pyrolysis which favors the formation of porous structure, S powder can offer sufficient sulfur source [48]. The excessive S element exists not only in the $Zn_{0.76}Co_{0.24}S$, ZnS and $Co_{1-x}S_x$

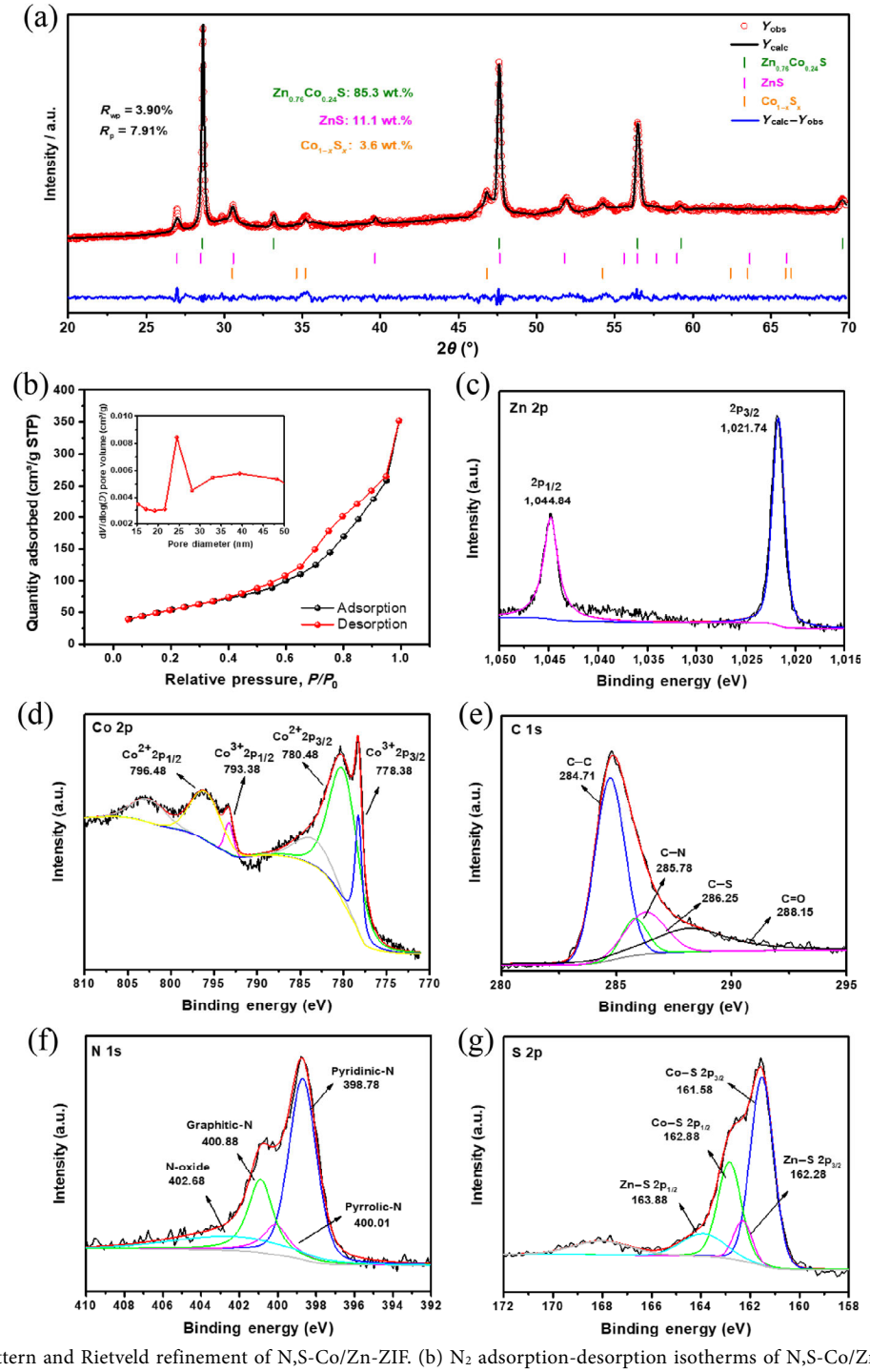

Figure 2 (a) XRD pattern and Rietveld refinement of N,S-Co/Zn-ZIF. (b) N_2 adsorption-desorption isotherms of N,S-Co/Zn-ZIF (inset: BJH pore size distribution profile). High-resolution XPS spectrum of (c) Zn 2p, (d) Co 2p, (e) C 1s, (f) N 1s, and (g) S 2p of the N,S-Co/Zn-ZIF, along with their corresponding fitting curves.

nanoparticles but also on the carbon surface, demonstrating the chemical contact between metal sulfur nanoparticles and the graphitized carbon layer which would greatly benefit to electrons transfer [49]. Noted that excessive sulfur may also lead to a defect which is favorable to the enhancement of electrocatalytic performance [50].

2.3 Electrocatalytic Behavior of as-synthesized electrocatalyst

The bimetallic ZIF-67 derived N,S-codoped porous carbon material N,S-Co/Zn-ZIF was used as electrocatalyst and investigated for electrochemical oxygen reactions. It was firstly characterized using linear sweep voltammetry (LSV) technique in KOH solution with a standard calomel electrode (SCE) as the reference. As shown by LSV profiles in Fig. 3(a), N,S-Co/Zn-ZIF exhibits a more positive onset potential of 0.96 V (vs. reversible hydrogen electrode, RHE), along with a significantly higher half-wave potential ($E_{1/2}$) of 0.86 V than those of any other materials for comparison, including N,S-Co-ZIF ($E_{1/2}$ = 0.76 V), N,S-Zn-ZIF ($E_{1/2}$ = 0.62 V), and Co/Zn-ZIF ($E_{1/2}$ = 0.73 V), for ORR process. Moreover, N,S-Co/Zn-ZIF exhibits comparable or even better ORR performance than commercial Pt/C electrocatalyst (Fig. S5(b) in the ESM) in terms of half-wave potential. It is believed that the existence of bimetallic Co and Zn leads to the formation of more hierarchical pores during high-temperature calcination, bringing more active sites for

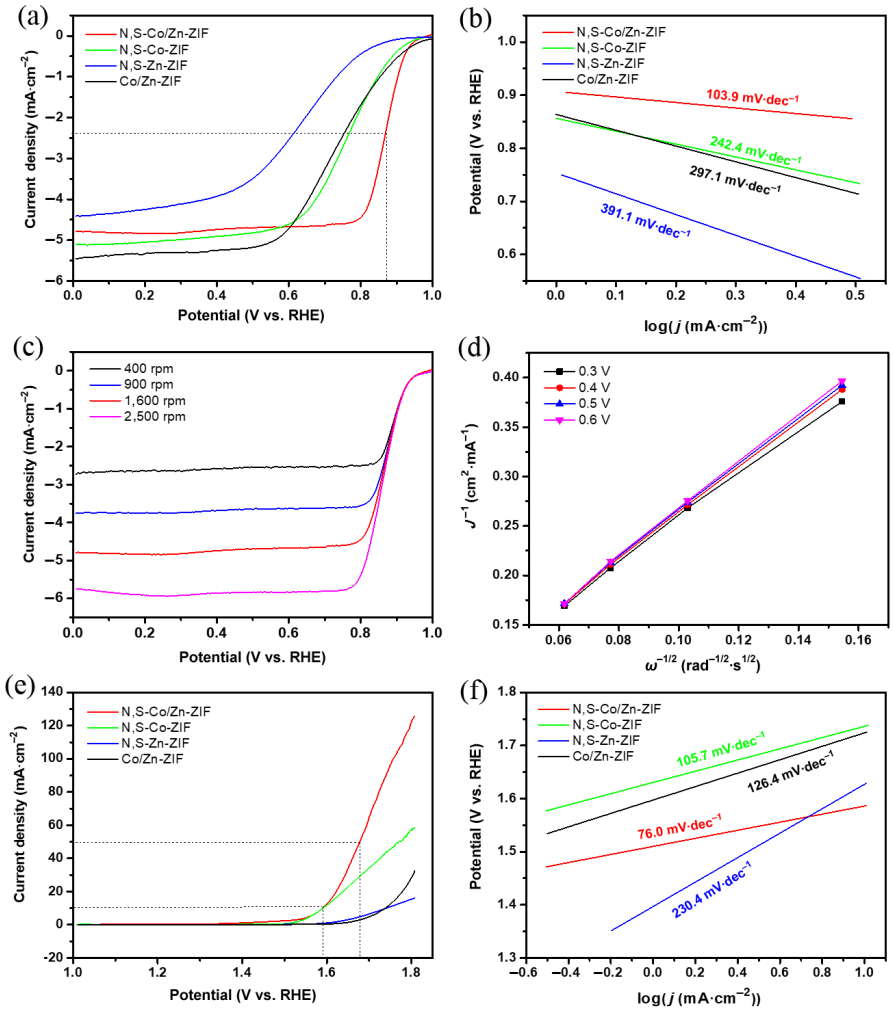

Figure 3 (a) Comparison of ORR polarization curves of N,S-Co/Zn-ZIF, N,S-Co-ZIF, N,S-Zn-ZIF and Co/Zn-ZIF electrocatalysts. (b) Corresponding Tafel plots of ORR with four electrocatalyst. (c) ORR polarization curves of N,S-Co/Zn-ZIF at different rotating speeds (400 to 2,500 rpm). (d) K-L plot of N,S-Co/Zn-ZIF. (e) OER polarization curves of N,S-Co/Zn-ZIF, N,S-Co-ZIF, N,S-Zn-ZIF and Co/Zn-ZIF electrocatalysts. (f) Corresponding Tafel plots of OER process with the four electrocatalysts.

sulfurization and prompt the formation of rough surfaces, as confirmed by N_2 sorption analysis and the XRD patterns of $Zn_{0.76}Co_{0.24}S$ and $Co_{1-x}S_x$. Moreover, S doping into the N-doped carbon alternates the surrounding electron density and hence increases the ORR activity of the electrocatalyst [12]. In addition, electrocatalytic activity is greatly enhanced due to the high content of pyridine N and graphite N, where these defects are created to provide abundant active sites [51, 52]. This result shows that the improved electrocatalytic ORR activity is dependent on a complex synergistic effect of higher and rougher surface area, graphitic N and pyridinic N. The notable ORR performance of N,S-Co/Zn-ZIF is further confirmed by the smaller Tafel slope of 103.9 mV·dec^{-1} at low overpotentials compared to that of N,S-Co-ZIF (242.4 mV·dec^{-1}), N,S-Zn-ZIF (391.1 mV·dec^{-1}) and Co/Zn-ZIF (297.1 mV·dec^{-1}) (Fig. 3(b)).

In order to further study the kinetic behavior, N,S-Co/Zn-ZIF was tested using LSV technique with the electrode at various rotating speeds (Fig. 3(c)). It can be clearly seen that as the rotating speed increases, the onset potential of N,S-Co/Zn-ZIF remains unchanged, while the current density increases sharply due to the improvement of mass transport and shortened diffusion distance. The electron transfer number per oxygen molecule (n) for ORR is determined from the LSV curves according to the Koutechy-Levich (K-L) equation. The K-L curves (Fig. 3(d)) display linear relationships between j_k^{-1} and $\omega^{-1/2}$ (where j_k is the kinetic current and ω is the electrode rotating rate), from which n was determined to be 3.94, suggesting a preferable four-electron pathway for ORR. By comparison, n values are calculated to be 3.78, 3.43 and 3.66 for N,S-Co-ZIF, N,S-Zn-ZIF and Co/Zn-ZIF, respectively (Fig. S6 in the ESM), suggesting a two-electron and four-electron mixed transfer pathway in ORR process.

In order to explore its bifunctional electrocatalytic behavior, the N,S-Co/Zn-ZIF and reference electrocatalysts are also investigated using LSV technique in OER process. LSV curves were obtained and compared at the rotating speed of 1,600 rpm at a scan rate of 10 mV·s^{-1}. As displayed in Fig. 3(e), N,S-Co/Zn-ZIF presents a significantly low onset potential (1.55 V) compared to N,S-Co-ZIF (1.56 V), N,S-Zn-ZIF (1.63 V) and Co/Zn-ZIF (1.65 V). Remarkably, N,S-Co/Zn-ZIF is found to possess the lowest overpotential (350 mV) and the best OER catalytic performance as it reaches 1.58 V at a current density of 10 mA·cm^{-2} after ZIR-correction (Fig. S5(a) in the ESM). This finding confirms that the OER performance of N,S-Co/Zn-ZIF is superior to that of the commercial RuO_2 electrocatalyst (Fig. S5(c) in the ESM). The corresponding Tafel plots of OER process for the various catalysts are shown in Fig. 3(f). The lower Tafel slope value of N,S-Co/Zn-ZIF (76.0 mV·dec^{-1}) indicates that its reaction is more kinetically favorable than

N,S-Co-ZIF (105.7 mV·dec^{-1}), N,S-Zn-ZIF (230.4 mV·dec^{-1}) and Co/Zn-ZIF (126.4 mV·dec^{-1}) (Fig. S6 in the ESM). The enhancement in OER performance can be ascribed to the ternary metal sulfides nanocrystals embedded in highly porous N and S co-doped carbon matrix. The hierarchical pores not only ensure a high surface area with exposed active sites but also open up transport channels facilitating fast access to them.

2.4 Discussion

To further understand such superior electrocatalytic performance of N,S-Co/Zn-ZIF, the electrochemical double-layer capacitance (C_{dl}) and electrochemical active surface area (ECSA) were estimated via cyclic voltammetry (CV) curves in the potential range of 0.968–1.068 V (vs. RHE) (Fig. S7 in the ESM). The C_{dl} of N,S-Co/ Zn-ZIF is determined to be 56.5734 mF·cm^{-2}, higher than that of N,S-Co-ZIF (55.8482 mF·cm^{-2}), N,S-Zn-ZIF (43.8338 mF·cm^{-2}), and Co/Zn-ZIF (47.2634 mF·cm^{-2}). This result is consistent with the N_2 sorption isotherms and reveals the presence of more exposed active sites in N,S-Co/Zn-ZIF which can be attributed to the N,S-doped carbon matrix. Furthermore, electrochemical impedance spectroscopy (EIS) measurements at a potential of 1.65 V (vs. RHE) is carried out for the discovery of the electrochemical kinetics and the internal resistance of different electrocatalytic materials. As can be seen in Fig. 4(a), N,S-Co/Zn-ZIF exhibits the smallest semi-circle, indicating the lowest resistance of electrolyte diffusion, the intrinsic resistance of the materials and the contact resistance between substrate and electrode materials [46]. This observation can be also explained by the open morphology, high specific surface area, abundant transport channels and active site of the N,S-Co/ Zn-ZIF nanostructure, which are in favor of the electrolyte diffusion during the electrochemical reaction processes. The N,S-Co/Zn-ZIF electrocatalyst was also tested at 0.51 V (vs. RHE) in O_2-saturated electrolyte for 60,000 s to measure the durability. Apparently, N,S-Co/Zn-ZIF displays stabler performance with larger current density at –2.7 mA·m^{-2}, whereas Pt/C catalyst electrode shows much higher current loss of 33.3% (Fig. 4(b)). Notably, after 60,000 s, the ORR performance of the N,S-Co/Zn-ZIF shows only a 5 mV decrease in half-wave potential which the limiting current stays constant with a value of –5 mA·cm^{-2} (Fig. S8(a) in the ESM). Long-term stability for OER process of N,S-Co/Zn-ZIF and the commercial RuO_2 is also tested at 1.71 V (vs. RHE) (Fig. 4(c)). N,S-Co/Zn-ZIF retains current density at 4.8 mA·cm^{-2} after 60,000 s which is much superior to the current density of RuO_2 (0.2 mA·cm^{-2}). The Fig. S8(b) in the ESM further confirms that after 60,000 s, the overpotential of N,S-Co/Zn-ZIF almost remain the same and the potential only increase 13 mV at limit current density of 50 mA·cm^{-2}. Obviously, N,S-Co/Zn-ZIF has excellent durability for electrochemical oxygen redox processes. First, high OER activity is likely dominated by metal-based species. Since Zn species is inactive in both OER and ORR, it creates more defects, thus it provides active and coordination sites during volatilization in high temperature. Second, the higher surface content of pyridinic N is favorable to afford the higher ORR mass and specific activities. Furthermore, the heteroatom sulfur doping on the carbon skeleton leads to an increase in charge population and density, acting as the extra active sites for ORR.

3 Conclusion

In conclusion, a novel nitrogen and sulfur atoms co-doped porous carbon nanostructure has been successfully achieved which is derived from bimetallic Co and Zn containing ZIF-67 structure. Such nanostructure possesses high surface area, highly porous feature, and excellent stable structure. When applied for electrochemical oxygen redox processes, it exhibits bifunctional catalytic behavior and outstanding electrocatalytic activity for both ORR and OER, where a high half-wave potential of 0.86 V (vs. RHE) and a limiting current density of –4.8 mA·cm^{-2} are achieved for ORR and a low overpotential of 350 mV is obtained in OER. Such excellent electrocatalytic performance is mainly due to the unique morphology and nanostructure. The material design is expected to open new directions in the synthesis and exploration of novel low cost and efficient electrocatalysts and it would further promote their wider applications in energy storage and conversion systems.

Acknowledgements

This work was financially supported by the Natural Sciences and Engineering Research Council of Canada (NSERC), through the Discovery Grant Program (RGPIN-2018-06725) and the Discovery Accelerator Supplement Grant program (RGPAS-2018-522651), and by the New Frontiers in Research Fund-Exploration program (NFRFE-2019-00488). L. C., Z. C. and X. L. W. also acknowledge support from Concordia University, the University of Alberta, and Future Energy Systems (FES). All authors thank Prof. Zhibin Ye for assistance in electrochemical measurements.

Electronic Supplementary Material: Supplementary material (detailed experimental procedures, additional TEM and SEM images for morphological studies, corresponding EDS results, XRD patterns and XPS analysis and electrochemical testing) is available in the online version of this article at https://doi.org/10.1007/s12274-020-3212-z.

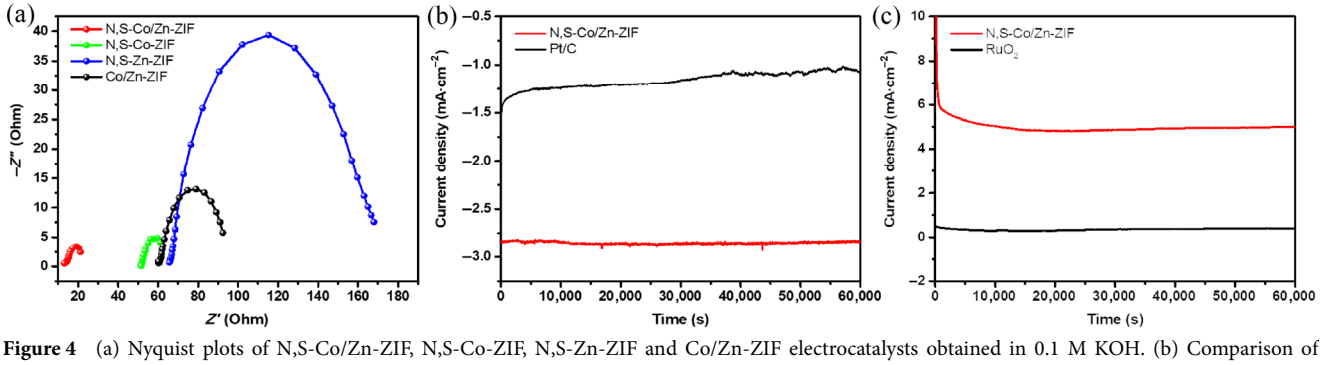

Figure 4 (a) Nyquist plots of N,S-Co/Zn-ZIF, N,S-Co-ZIF, N,S-Zn-ZIF and Co/Zn-ZIF electrocatalysts obtained in 0.1 M KOH. (b) Comparison of chronoamperometric responses for ORR process between N,S-Co/Zn-ZIF and Pt/C at 0.51 V in 0.1 M KOH (vs. RHE). (c) Comparison of chronoamperometric responses for OER process between N,S-Co/Zn-ZIF and RuO_2 at 1.71 V in 1 M KOH (vs. RHE).

References

[1] Elizabeth, I.; Nair, A. K.; Singh, B. P.; Gopukumar, S. Multifunctional Ni-Nio-CNT composite as high performing free standing anode for Li ion batteries and advanced electro catalyst for oxygen evolution reaction. *Electrochim. Acta* **2017**, *230*, 98–105.

[2] Lee, S. H.; Jo, Y. R.; Noh, Y.; Kim, B. J.; Kim, W. B. Fabrication of hierarchically branched SnO_2 nanowires by two-step deposition method and their applications to electrocatalyst support and Li ion electrode. *J. Power Sources* **2017**, *367*, 1–7.

[3] Yu, W. T.; Shang, W. X.; Tan, P.; Chen, B.; Wu, Z.; Xu, H. R.; Shao, Z. P.; Liu, M. L.; Ni, M. Toward a new generation of low cost, efficient, and durable metal-air flow batteries. *J. Mater. Chem. A* **2019**, *7*, 26744–26768.

[4] Yao, R. Q.; Shi, H.; Wan, W. B.; Wen, Z.; Lang, X. Y.; Jiang, Q. Flexible Co-Mo-N/Au electrodes with a hierarchical nanoporous architecture as highly efficient electrocatalysts for oxygen evolution reaction. *Adv. Mater.* **2020**, *32*, 1907214.

[5] Gebremariam, T. T.; Chen, F. Y.; Jin, Y. C.; Wang, Q.; Wang, J. L.; Wang, J. P. Bimetallic NiCo/CNF encapsulated in a N-doped carbon shell as an electrocatalyst for Zn-air batteries and water splitting. *Catal. Sci. Technol.* **2019**, *9*, 2532–2542.

[6] Song, S. D.; Li, W. J.; Deng, Y. P.; Ruan, Y. L.; Zhang, Y. N.; Qin, X. H.; Chen, Z. W. TiC supported amorphous MnO_x as highly efficient bifunctional electrocatalyst for corrosion resistant oxygen electrode of Zn-air batteries. *Nano Energy* **2020**, *67*, 104208.

[7] Shi, F.; Zhu, X. F.; Yang, W. S. Micro-nanostructural designs of bifunctional electrocatalysts for metal-air batteries. *Chin. J. Catal.* **2020**, *41*, 390–403.

[8] Kim, M.; Ju, H.; Kim, J. Dihydrogen phosphate ion functionalized nanocrystalline thallium ruthenium oxide pyrochlore as a bifunctional electrocatalyst for aqueous Na-air batteries. *Appl. Catal. B Environ.* **2019**, *245*, 29–39.

[9] Antolini, E. Iridium as catalyst and cocatalyst for oxygen evolution/reduction in acidic polymer electrolyte membrane electrolyzers and fuel cells. *ACS Catal.* **2014**, *4*, 1426–1440.

[10] Wang, X. X.; Sunarso, J.; Lu, Q.; Zhou, Z. L.; Dai, J.; Guan, D. Q.; Zhou, W.; Shao, Z. P. High-performance platinum-perovskite composite bifunctional oxygen electrocatalyst for rechargeable Zn-air battery. *Adv. Energy Mater.* **2020**, *10*, 1903271.

[11] Xiao, X.; Li, X. H.; Wang, Z. X.; Yan, G. C.; Guo, H. J.; Hu, Q. Y.; Li, L. J.; Liu, Y.; Wang, J. X. Robust template-activator cooperated pyrolysis enabling hierarchically porous honeycombed defective carbon as highly-efficient metal-free bifunctional electrocatalyst for Zn-air batteries. *Appl. Catal. B Environ.* **2020**, *265*, 118603.

[12] Guo, J. R.; Yu, Y.; Ma, J. C.; Zhang, T. T.; Xing, S. X. Facile route to achieve N,S-codoped carbon as bifunctional electrocatalyst for oxygen reduction and evolution reactions. *J. Alloys Compd.* **2020**, *821*, 153484.

[13] Cui, C. H.; Gan, L.; Li, H. H.; Yu, S. H.; Heggen, M.; Strasser, P. Octahedral PtNi nanoparticle catalysts: Exceptional oxygen reduction activity by tuning the alloy particle surface composition. *Nano Lett.* **2012**, *12*, 5885–5889.

[14] Parra-Puerto, A.; Ng, K. L.; Fahy, K.; Goode, A. E.; Ryan, M. P.; Kucernak, A. Supported transition metal phosphides: Activity survey for HER, ORR, OER, and corrosion resistance in acid and alkaline electrolytes. *ACS Catal.* **2019**, *9*, 11515–11529.

[15] Chen, D.; Zhu, J. W.; Mu, X. Q.; Cheng, R. L.; Li, W. Q.; Liu, S. L.; Pu, Z. H.; Lin, C.; Mu, S. C. Nitrogen-doped carbon coupled $FeNi_3$ intermetallic compound as advanced bifunctional electrocatalyst for OER, ORR and Zn-air batteries. *Appl. Catal. B Environ.***2020**, *268*, 118729.

[16] He, X.; Luan, S. Z.; Wang, L.; Wang, R. Y.; Du, P.; Xu, Y. Y.; Yang, H. J.; Wang, Y. G.; Huang, K.; Lei, M. Facile loading mesoporous Co_3O_4 on nitrogen doped carbon matrix as an enhanced oxygen electrode catalyst. *Mater. Lett.* **2019**, *244*, 78–82.

[17] Li, G.; Wang, X. L.; Fu, J.; Li, J. D.; Park, M. G.; Zhang, Y. N.; Lui, G.; Chen, Z. W. Pomegranate-inspired design of highly active and durable bifunctional electrocatalysts for rechargeable metal-air batteries. *Angew. Chem., Int. Ed.* **2016**, *55*, 4977–4982.

[18] Xia, S. B.; Yu, S. W.; Yao, L. F.; Li, F. S.; Li, X.; Cheng, F. X.; Shen, X.; Sun, C. K.; Guo, H.; Liu, J. J. Robust hexagonal nut-shaped titanium (IV) MOF with porous structure for ultra-high performance lithium storage. *Electrochim. Acta* **2019**, *296*, 746–754.

[19] Jayaramulu, K.; Dubal, D. P.; Schneemann, A.; Ranc, V.; Perez-Reyes, C.; Stráská, J.; Kment, Š.; Otyepka, M.; Fischer, R. A.; Zbořil, R. Shape-assisted 2D MOF/graphene derived hybrids as exceptional lithium-ion battery electrodes. *Adv. Funct. Mater.* **2019**, *29*, 1902539.

[20] Yu, S. Z.; Luo, S. H.; Zhan, Y.; Huang, H. B.; Wang, Q.; Zhang, Y. H.; Liu, Y. G.; Hao, A. I. Metal-organic framework-derived cobalt nanoparticle space confined in nitrogen-doped carbon polyhedra networks as high-performance bifunctional electrocatalyst for rechargeable Li-O_2 batteries. *J. Power Sources* **2020**, *453*, 227899.

[21] Chen, D.; Yu, J. H.; Cui, Z. X.; Zhang, Q.; Chen, X.; Sui, J.; Dong, H. Z.; Yu, L. Y.; Dong, L. F. Hierarchical architecture derived from two-dimensional zeolitic imidazolate frameworks as an efficient metal-based bifunctional oxygen electrocatalyst for rechargeable Zn-air batteries. *Electrochim. Acta* **2020**, *331*, 135394.

[22] Guan, Y.; Li, Y. L.; Luo, S.; Ren, X. Z.; Deng, L. B.; Sun, L. N.; Mi, H. W.; Zhang, P. X.; Liu, J. H. Rational design of positive-hexagon-shaped two-dimensional ZIF-derived materials as improved bifunctional oxygen electrocatalysts for use as long-lasting rechargeable Zn-air batteries. *Appl. Catal. B Environ.* **2019**, *256*, 117871.

[23] Li, Z. Y.; Liu, H. D.; Huang, J. M.; Zhang, L. MOF-derived α-MnSe/C composites as anode materials for Li-ion batteries. *Ceram. Int.* **2019**, *45*, 23765–23771.

[24] Duan, J. L.; Zou, Y. L.; Li, Z. Y.; Long, B. Preparation of MOF-derived NiCoP nanocages as anodes for lithium ion batteries. *Powder Technol.* **2019**, *354*, 834–841.

[25] Wang, C. C.; Hung, K. Y.; Ko, T. E.; Hosseini, S.; Li, Y. Y. Carbon-nanotube-grafted and nano-Co_3O_4-doped porous carbon derived from metal-organic framework as an excellent bifunctional catalyst for zinc-air battery. *J. Power Sources* **2020**, *452*, 227841.

[26] Chen, D.; Chen, X.; Cui, Z. X.; Li, G. F.; Han, B.; Zhang, Q.; Sui, J.; Dong, H. Z.; Yu, J. H.; Yu, L. Y. et al. Dual-active-site hierarchical architecture containing NiFe-LDH and ZIF-derived carbon-based framework composite as efficient bifunctional oxygen electrocatalysts for durable rechargeable Zn-air batteries. *Chem. Eng. J.* **2020**, *399*, 125718.

[27] Wang, Q.; Shang, L.; Shi, R.; Zhang, X.; Zhao, Y. F.; Waterhouse, G. I. N.; Wu, L. Z.; Tung, C. H.; Zhang, T. R. NiFe layered double hydroxide nanoparticles on Co, N-codoped carbon nanoframes as efficient bifunctional catalysts for rechargeable zinc-air batteries. *Adv. Energy Mater.* **2017**, *7*, 1700467.

[28] Li, Y. L.; Jia, B. M.; Fan, Y. Z.; Zhu, K. L.; Li, G. Q.; Su, C. Y. Bimetallic zeolitic imidazolite framework derived carbon nanotubes embedded with Co nanoparticles for efficient bifunctional oxygen electrocatalyst. *Adv. Energy Mater.* **2018**, *8*, 1702048.

[29] Guo, J. X.; Gao, M.; Nie, J.; Yin, F. X.; Ma, G. P. ZIF-67/PAN-800 bifunctional electrocatalyst derived from electrospun fibers for efficient oxygen reduction and oxygen evolution reaction. *J. Colloid Interface Sci.* **2019**, *544*, 112–120.

[30] Khalid, M.; Honorato, A. M. B.; Ticianelli, E. A.; Varela, H. Uniformly self-decorated Co_3O_4 nanoparticles on N, S co-doped carbon layers derived from a camphor sulfonic acid and metal-organic framework hybrid as an oxygen evolution electrocatalyst. *J. Mater. Chem. A* **2018**, *6*, 12106–12114.

[31] Hang, C.; Zhang, J.; Zhu, J.; Li, W.; Kou, Z.; Huang, Y. *In situ* exfoliating and generating active sites on graphene nanosheets strongly coupled with carbon fiber toward self-standing bifunctional cathode for rechargeable Zn-air batteries. *Adv. Energy Mater.* **2018**, *8*, 1703539.

[32] Wei, J.; Hu, Y. X.; Liang, Y.; Kong, B.; Zhang, J.; Song, J. C.; Bao, Q. L.; Simon, G. P.; Jiang, S. P.; Wang, H. T. Nitrogen-doped nanoporous carbon/graphene nano-sandwiches: Synthesis and application for efficient oxygen reduction. *Adv. Funct. Mater.* **2015**, *25*, 5768–5777.

[33] Chen, Z. L.; Liu, M.; Wu, R. B. Strongly coupling of Co_9S_8/Zn-Co-S heterostructures rooted in carbon nanocages towards efficient oxygen evolution reaction. *J. Catal.* **2018**, *361*, 322–330.

[34] Guan, C.; Xiao, W.; Wu, H. J.; Liu, X. M.; Zang, W. J.; Zhang, H.; Ding, J.; Feng, Y. P.; Pennycook, S. J.; Wang, J. Hollow Mo-doped CoP nanoarrays for efficient overall water splitting. *Nano Energy* **2018**, *48*, 73–80.

[35] Zeng, K.; Su, J. M.; Cao, X. C.; Zheng, X. J.; Li, X. W. ; Tian, J. H.;

Jin, C.; Yang, R. Z. B, N Co-doped ordered mesoporous carbon with enhanced electrocatalytic activity for the oxygen reduction reaction. *J. Alloys Compd.* **2020**, *824*, 153908.

[36] Shao, Q.; Liu, J. Q.; Wu, Q.; Li, Q.; Wang, H. G.; Li, Y. H.; Duan, Q. *In situ* coupling strategy for anchoring monodisperse Co_9S_8 nanoparticles on S and N dual-doped graphene as a bifunctional electrocatalyst for rechargeable Zn-air battery. *Nano-Micro Lett.* **2019**, *11*, 4.

[37] Li, K. L.; Li, D. H.; Zhu, L. K.; Gao, Z. Z.; Fang, Q. R.; Xue, M.; Qiu, S. L.; Yao, X. D. Bimetallic ZIF derived Co nanoparticle anchored N-doped porous carbons for an efficient oxygen reduction reaction. *Inorg. Chem. Front.* **2020**, *7*, 946–952.

[38] Jin, H. H.; Zhou, H.; Li, W. Q.; Wang, Z. H.; Yang, J. L.; Xiong, Y. L.; He, D. P.; Chen, L.; Mu, S. C. *In situ* derived Fe/N/S-codoped carbon nanotubes from ZIF-8 crystals as efficient electrocatalysts for the oxygen reduction reaction and zinc-air batteries. *J. Mater. Chem. A* **2018**, *6*, 20093–20099.

[39] Wang, R.; Dong, X. Y.; Du, J.; Zhao, J. Y.; Zang, S. Q. MOF-derived bifunctional Cu_3P nanoparticles coated by a N, P-codoped carbon shell for hydrogen evolution and oxygen reduction. *Adv. Mater.* **2018**, *30*, 1703711.

[40] Chen, B. H.; He, X. B.; Yin, F. X.; Wang, H.; Liu, D. J.; Shi, R. X.; Chen, J. N.; Yin, H. W. MO-Co@N-doped carbon (M = Zn or Co): Vital roles of inactive Zn and highly efficient activity toward oxygen reduction/evolution reactions for rechargeable Zn-air battery. *Adv. Funct. Mater.* **2017**, *27*, 1700795.

[41] He, W. D.; Wang, C. G.; Li, H. Q.; Deng, X. L.; Xu, X. J.; Zhai, T. Y. Ultrathin and porous Ni_3S_2/$CoNi_2S_4$ 3D-network structure for superhigh energy density asymmetric supercapacitors. *Adv. Energy Mater.* **2017**, *7*, 1700983.

[42] Yang, Y.; Li, S.; Huang, W.; Shangguan, H. H.; Engelbrekt, C.; Duan, S. W.; Ci, L. J.; Si, P. Effective synthetic strategy for $Zn_{0.76}Co_{0.24}S$ encapsulated in stabilized N-doped carbon nanoarchitecture towards ultra-long-life hybrid supercapacitors. *J. Mater. Chem. A* **2019**, *7*, 14670–14680.

[43] Yin, X. J.; Sun, W. W.; Lv, L. P.; Wang, Y. Boosting lithium-ion storage performance by synergistically coupling $Zn_{0.76}Co_{0.24}S$ with N-/S-doped carbon and carbon nanofiber. *Chem. Eng. J.* **2018**, *346*, 376–387.

[44] Zhou, Y.; Leng, Y.; Zhou, W.; Huang, J.; Zhao, M.; Zhan, J.; Feng, C.; Tang, Z.; Chen, S.; Liu, H. Sulfur and nitrogen self-doped carbon nanosheets derived from peanut root nodules as high-efficiency non-metal electrocatalyst for hydrogen evolution reaction. *Nano Energy* **2015**, *16*, 357–366.

[45] Amiinu, I. S.; Pu, Z. H.; Liu, X. B.; Owusu, K. A.; Monestel, H. G. R.; Boakye, F. O.; Zhang, H. N.; Mu, S. C. Multifunctional Mo-N/C@MoS_2 electrocatalysts for HER, OER, ORR, and Zn-air batteries. *Adv. Funct. Mater.* **2017**, *27*, 1702300.

[46] Wang, X.; Ma, Z. J.; Chai, L. L.; Xu, L. Q.; Zhu, Z. Y.; Hu, Y.; Qian, J. J.; Huang, S. M. MOF derived N-doped carbon coated CoP particle/carbon nanotube composite for efficient oxygen evolution reaction. *Carbon* **2019**, *141*, 643–651.

[47] Zhang, S. L.; Guan, B. Y.; Lou, X. W. D. Co-Fe alloy/N-doped carbon hollow spheres derived from dual metal-organic frameworks for enhanced electrocatalytic oxygen reduction. *Small* **2019**, *15*, 1805324.

[48] Yang, Y.; Huang, W.; Li, S.; Ci, L. J.; Si, P. C. Surfactant-dependent flower- and grass-like $Zn_{0.76}Co_{0.24}S$/Co_3S_4 for high-performance all-solid-state asymmetric supercapacitors. *J. Mater. Chem. A* **2018**, *6*, 22830–22839.

[49] Zhao, Y. H.; Dong, H. X.; He, X. Y.; Yu, J.; Chen, R. R.; Liu, Q.; Liu, J. Y.; Zhang, H. S.; Li, R. M.; Wang, J. Design of 2D mesoporous Zn/Co-based metal-organic frameworks as a flexible electrode for energy storage and conversion. *J. Power Sources* **2019**, *438*, 227057.

[50] Cao, Q. C.; Ding, X. B.; Li, F.; Qin, Y. H.; Wang, C. Zinc, sulfur and nitrogen co-doped carbon from sodium chloride/zinc chloride-assisted pyrolysis of thiourea/sucrose for highly efficient oxygen reduction reaction in both acidic and alkaline media. *J. Colloid Interface Sci.* **2020**, *576*, 139–146.

[51] Zhang, S. L.; Zhai, D.; Sun, T. T.; Han, A. J.; Zhai, Y. L.; Cheong, W. C.; Liu, Y.; Su, C. L.; Wang, D. S.; Li, Y. D. *In situ* embedding Co_9S_8 into nitrogen and sulfur codoped hollow porous carbon as a bifunctional electrocatalyst for oxygen reduction and hydrogen evolution reactions. *Appl. Catal. B Environ.* **2019**, *254*, 186–193.

[52] Yang, L. F.; Zhang, L.; Xu, G. C.; Ma, X.; Wang, W. W.; Song, H. J.; Jia, D. Z. Metal-organic-framework-derived hollow CoS_x@MoS_2 microcubes as superior bifunctional electrocatalysts for hydrogen evolution and oxygen evolution reactions. *ACS Sustainable Chem. Eng.* **2018**, *6*, 12961–12968.

[53] Liu, Y. S.; Shen, H. B.; Jiang, H.; Li, W. Z.; Li, J.; Li, Y. M.; Guo, Y. ZIF-derived graphene coated/Co_9S_8 nanoparticles embedded in nitrogen doped porous carbon polyhedrons as advanced catalysts for oxygen reduction reaction. *Int. J. Hydrog. Energy* **2017**, *42*, 12978–12988.

[54] Wang, J. L.; Liu, H.; Liu, Y.; Wang, W. H.; Sun, Q.; Wang, X. B.; Zhao, X. Y.; Hu, H.; Wu, M. B. Sulfur bridges between Co_9S_8 nanoparticles and carbon nanotubes enabling robust oxygen electrocatalysis. *Carbon* **2019**, *144*, 259–268.